Resolving correlated states of benzyne with an error-mitigated contracted quantum eigensolver

Scott E. Smart ⬤, Jan-Niklas Boyn ⬤, and David A. Mazziotti ⬤[*]

Department of Chemistry and The James Franck Institute, The University of Chicago, Chicago, Illinois 60637, USA

The simulation of strongly correlated many-electron systems is one of the most promising applications for near-term quantum devices. Here we use a class of eigenvalue solvers [presented in Smart and Mazziotti, Phys. Rev. Lett. **126**, 070504 (2021)] in which a contraction of the Schrödinger equation is solved for the two-electron reduced density matrix (2-RDM) to resolve the energy splittings of the *ortho-*, *meta-*, and *para-*isomers of benzyne C_6H_4. In contrast to the traditional variational quantum eigensolver, the contracted quantum eigensolver can solve an integration (or contraction) of the many-electron Schrödinger equation onto the two-electron space. The quantum solution of the anti-Hermitian part of the contracted Schrödinger equation provides a scalable approach with few variational parameters that has its foundations in 2-RDM theory. Experimentally, a variety of error-mitigation strategies enable the calculation, including a linear shift in the 2-RDM targeting the iterative nature of the algorithm as well as a projection of the 2-RDM onto the convex set of approximately N-representable 2-RDMs defined by the 2-positive N-representability conditions. The relative energies exhibit single-digit millihartree errors, capturing a large part of the electron correlation energy, and the computed natural orbital occupations reflect the significant differences in the electron correlation of the isomers.

I. INTRODUCTION

The simulation of many-body quantum systems is a key application for near-term quantum computing [1–4]. The complexity of these simulations is such that algorithms on even moderately sized quantum devices, comprised of tens of qubits, with sufficient error mitigation will likely be competitive with existing classical methods [5–8]. A particular instance is the simulation of strongly correlated molecular systems, such as occur in many chemical reactions, transition-metal complexes, energetically degenerate processes, and solid-state materials [9–11]. These systems, which often cannot be treated consistently with perturbative or polynomially scaling approaches relying on a single determinant, are ideal candidates for realizing an advantage from the use of quantum computers in lieu of classical computers, known as quantum advantage. Realizing such advantage, however, requires algorithms that are optimal for quantum computers in terms of state preparation, measurement, and error mitigation for the noise present in near-to-intermediate-term devices [12,13].

Various variational quantum eigensolvers (VQE) for molecular simulation exist [14–21], most of which attempt to minimize the energy of a parametrizable *Ansatz* against the Schrödinger equation. An alternative family of algorithms known as contracted quantum eigensolvers (CQE) [22] involves minimizing the residual of a projection (or contraction) of the N-electron Schrödinger equation onto the space of two electrons, known as the contracted Schrödinger equation (CSE) [23–30]. Closely connected to classical reduced density matrix theory, the CQE has several key features

that are favorable to efficient quantum molecular simulations. First, the solution of the CSE, it has been shown, produces an exact, rapidly convergent parametrization of the wave function from a product of only two-body exponential transformations [31,32]. Furthermore, solution of the anti-Hermitian part of the CSE, known as the anti-Hermitian CSE (ACSE) [33–36], can yield a parametrization of the wave function in terms of two-body unitary transformations [33,35], which is theoretically exact [37] and readily implementable through unitary gates for state preparation on a quantum computer. Second, the residual of the ACSE yields the gradient of the energy with respect to two-body unitary transformations, which allows for more efficient optimization on quantum computers than derivative-free schemes [14,38–41] that could be limited to hundreds of parameters. Indeed, recent work by our group introduced a CQE algorithm which can solve the ACSE efficiently on a quantum computer [22].

Solution of the ACSE for the two-electron reduced density matrix (2-RDM) on classical computers has been applied to treating both ground and excited states of strongly correlated molecules including nontrivial conical intersections [35,42–48]. The solution of the ACSE on quantum computers, a CQE algorithm or quantum ACSE, can potentially avoid the approximate reconstruction of the 3-electron reduced density matrix (3-RDM) from the 2-RDM through preparation of the wave function on the quantum computer in polynomial time [49]. The quantum ACSE also shares certain similarities with the methods that attempt to decouple and expand the single exponential unitary coupled cluster (UCC) *Ansatz* [50,51], such as the adaptive derivative-assembled pseudo-Trotterization VQE (ADAPT-VQE) method [52]. The quantum ACSE circumvents issues of the Trotterization of the *Ansatz* (necessary for an exact exponential expression) and
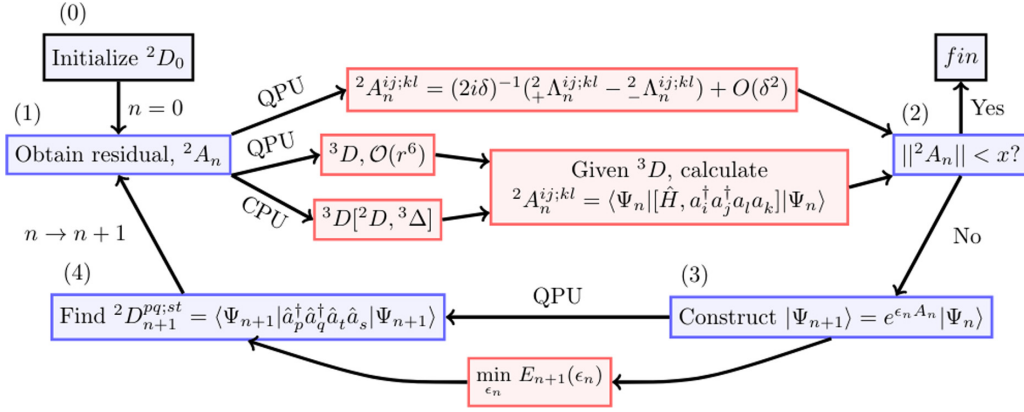
---

*[*]damazz@uchicago.edu

FIG. 1. The quantum-ACSE algorithm. After initializing the state (0), we begin an iterative process of obtaining the ^2A elements (1) using a quantum (QPU) or classical (CPU) processor, which will have errors in the series expansion $[O(\delta^2)]$, a higher measurement cost $[O(r^6)]$, or errors from the three-electron reduced cumulant matrix ($^3\Delta$). After checking for convergence against a threshold x (2), we construct the next *Ansatz* (3), and optionally perform a classical minimization against the step size. Finally, we measure the new 2-RDM (4), and proceed to (1) until we converge or $n = n_{\max}$.

high variational cost involved in an update step, and contains a natural selection of a pool of unitary transformations through the elements of the ACSE. Moreover, because the ACSE generates the 2-RDM, it is readily combined with error-mitigation strategies that correct the N-representability of the 2-RDM. With its theoretical advantages and promising computational results, the ACSE method provides a potentially flexible framework for molecular simulation on quantum computers.

In this work we apply the quantum ACSE solver to resolve the relative ground-state energies of the correlated isomers of benzyne on a superconducting quantum computer. The *ortho-*, *meta-*, and *para*-benzyne (C_6H_4) isomers contain nontrivial electron correlation, especially *para*-benzyne which is a biradical [53–58]. The computed relative energies are accurate to less than 0.005 hartrees, and the natural-orbital occupations reflect the differences in electron correlation among the isomers. The accuracy of the results demonstrates the benefits of both the solver and the error-mitigation strategies. Because these strategies are general, they can be applied to larger, more correlated molecules and represent a step towards performing strongly correlated calculations on a quantum computer

II. THEORY

In this section we review the theoretical framework for the quantum ACSE algorithm [22], and explore the error-mitigation schemes necessary for the calculation, including the use of N-representability conditions for the purification of the measured 2-RDM [59,60].

A. Quantum solver of the anti-Hermitian contracted Schrödinger equation

For a many-electron system the two-electron contracted Schrödinger equation [23–30] is

$$\langle\Psi|\hat{a}_i^\dagger\hat{a}_j^\dagger\hat{a}_l\hat{a}_k\hat{H}|\Psi\rangle = E\,{}^2D_{kl}^{ij}, \tag{1}$$

where ^2D is the 2-RDM, $\hat{a}_i^\dagger$ and $\hat{a}_i$ are creation and annihilation operators for a spin orbital i, and $\hat{H}$ is the Hamiltonian

operator that is given by

$$\hat{H} = \sum_{pqst} {}^2K_{st}^{pq}\hat{a}_p^\dagger\hat{a}_q^\dagger\hat{a}_t\hat{a}_s, \tag{2}$$

in which ^2K is the reduced Hamiltonian matrix containing the one- and two-electron integrals. Taking the anti-Hermitian part of Eq. (1) produces the ACSE [33–35,46,47]

$$\langle\Psi|[\hat{a}_i^\dagger\hat{a}_j^\dagger\hat{a}_l\hat{a}_k, \hat{H}]|\Psi\rangle = 0, \tag{3}$$

which depends upon not only the 2-RDM but also the three-electron RDM (3-RDM) (see Refs. [34,61,62] and Appendix B 4). The residual of the ACSE is equal to the gradient of the energy with respect to two-body unitary transformations and, hence, the residual of the ACSE vanishes if and only if the gradient vanishes. Consequently, the ACSE provides a framework for the iterative optimization of a product of two-body unitary transformations on a reference wave function, which leads to the quantum ACSE algorithm presented in Fig. 1.

Let $|\Psi_n\rangle$ be the nth iteration of the wave function, where $^2D_0$ is the 2-RDM of the initial Hartree-Fock state $|\Psi_0\rangle$. The 2-RDM of the $(n+1)$th iteration is

$$^2D_{n+1}^{pq;st} = \langle\Psi_n|e^{-\epsilon_n\hat{A}_n}\hat{a}_p^\dagger\hat{a}_q^\dagger\hat{a}_t\hat{a}_s e^{\epsilon_n\hat{A}_n}|\Psi_n\rangle, \tag{4}$$

where ϵ_n is theoretically an infinitesimal step and $\hat{A}_n$ is an anti-Hermitian operator

$$\hat{A}_n = \sum_{ijkl} {}^2A_n^{ij;kl}\hat{a}_i^\dagger\hat{a}_j^\dagger\hat{a}_l\hat{a}_k. \tag{5}$$

The energy at each iteration is computable from the 2-RDM

$$E_{n+1} = \sum_{pqst} {}^2K_{st}^{pq}\,{}^2D_{n+1}^{pq;st}. \tag{6}$$

Elements of the ^2A_n matrix can be selected [34] as the residual of the ACSE:

$$^2A_n^{ij;kl} = \langle\Psi_n|[\hat{a}_i^\dagger\hat{a}_j^\dagger\hat{a}_l\hat{a}_k, \hat{H}]|\Psi_n\rangle, \tag{7}$$

which is effective because the ACSE's residual is related to the gradient of the energy with respect to the elements of ^2A_n:

$$\langle\Psi_n|[\hat{a}_i^\dagger\hat{a}_j^\dagger\hat{a}_l\hat{a}_k,\hat{H}]|\Psi_n\rangle = -\frac{1}{\epsilon_n}\frac{\partial E_{n+1}}{\partial\,^2A_n^{ij;kl}} + O(\epsilon_n). \quad (8)$$

Hence, by using the residual, we are choosing a search direction that maximizes the change in the energy for small ϵ_n. The ACSE can be expressed in terms of the 2- and 3-RDMs and can be evaluated classically with an $O(r^6)$ cost using a reconstructed 3-RDM in which r is the rank of the one-electron basis set. On a quantum computer, we can obtain elements of ^2A_n in a potentially more efficient manner without the reconstructed 3-RDM. Define an auxiliary 2-RDM:

$$^2_\pm\Lambda_n^{ij;kl} = \langle\Psi_n|e^{\mp i\delta\hat{H}}\hat{a}_i^\dagger\hat{a}_j^\dagger\hat{a}_l\hat{a}_k e^{\pm i\delta\hat{H}}|\Psi_n\rangle, \quad (9)$$

in which the nth wave function is propagated through a time-like step δ in the forward or reverse direction. Then, we can obtain elements of the residual from tomography of these auxiliary RDMs with $O(r^4)$ scaling:

$$^2A_n^{ij;kl} = \frac{1}{2i\delta}\left(^2_+\Lambda_n^{ij;kl} - ^2_-\Lambda_n^{ij;kl}\right) + O(\delta^2). \quad (10)$$

These equations suggest an iterative approach to finding a solution of the ACSE, which is depicted in Fig. 1. After initializing the wave function and 2-RDM, for a given iteration we construct the matrix ^2A_n through classical or quantum approaches, prepare and measure $^2D_{n+1}$ (possibly optimizing ϵ_n and carefully selecting elements of ^2A_n to include in the wave function), and iterate between $^2D_{n+1}$ and ^2A_n until $||\,^2A_n||$ is less than a certain threshold.

In the classical-computing algorithm the solution of the ACSE requires an approximate reconstruction of the 3-RDM from the 2-RDM through a cumulant expansion [61,63,64] to compute the 2-RDM without the wave function. In the quantum-computing algorithm, in contrast, the wave function is prepared with polynomial scaling and, hence, approximate reconstruction of the 3-RDM is not necessary. A hybrid quantum-classical approach exists as well, where we prepare the wave function and measure the RDMs on the quantum computer but evaluate the ACSE for the residual (gradient) on the classical computer. In the noiseless limit the ACSE can be solved by the quantum-computing algorithm to an arbitrary level of accuracy. The errors arising from the expansion in Eq. (6) are controllable with respect to δ. Computationally, we find in the noiseless limit that the solution of the ACSE yields a wave function, parametrized by two-body unitary transformations, that solves not only the ACSE but also the N-electron Schrödinger equation.

Finally, several variations of the algorithm are possible for practical implementations on quantum computers. For example, a limited portion of ^2A_n, such as its largest terms, can be used; a stochastic gradient or reduced gradient sampling technique can be implemented, lowering the measurement cost of $^2\Lambda_n$ at each step. The quantum and classical methods can be combined where direct quantum tomography is only employed for the parts of the 2-RDM that are strongly correlated.

B. Quantum computation

In this work we utilize the QACSE method and generate ^2D_n on the quantum computer, and obtain elements of ^2A_n on the quantum computer for the smaller qubit calculations [Eq. (10)], and classically with a reconstructed 3-RDM for the larger qubit calculations [Eq. (8)]. Figure 2 provides an overview of the process to obtain a fully error mitigated ^2D_n. We also include details related to the specific techniques and other aspects of the calculation in Appendix B.

To obtain ^2D_n, at a given step, we first transform the $\hat{A}_n$ operator into a suitable form for the quantum computer (including our qubit reduction scheme). Explicitly, this is done through a first-order Trotterization of the exponential of Eq. (5), where each element of the ^2A_n matrix is implemented separately. However, because we would like to avoid implementing all the operators at once, we use an element threshold to determine inclusion in the *Ansatz*. To implement the gate sequence, we prepare and manually simplify the set of 2-RDM operators corresponding with possible elements of ^2A_n. These are assembled according to our inclusion criteria, and then the circuits are run. After measurement, we apply a filter (via construction and inversion of a state transition matrix, referred to as SPAM) and then apply a projection into the proper number and projected spin space ($N \in \{2, 4\}$, $S_z = 0$) for measurements which commutes with these operators (which are Z_i-type measurements). In some cases we then apply our limit-preserving correction Γ_n to the *Ansatz* (see below), followed by an optional purification of the 2-RDM.

To our knowledge, the penultimate error-mitigation technique has not been used elsewhere, and the final technique was recently introduced for quantum simulations [60] but not yet demonstrated experimentally, and so we briefly detail them here. The first is a correction targeting errors in an iterative *Ansatz* that arise simply from adding extra gates, whereas the second is an expansion of techniques related to ensuring the physicality of the measured RDM through N-representability constraints.

C. Limit-preserving correction for an iterative *Ansatz*

To compensate for errors which occur at each step due to the increasing number of gates in an iterative scheme, we present an error-mitigation strategy which we call a limit-preserving correction or a $^2\Gamma$ correction. Consider the nth iteration of the QACSE algorithm. Given the elements of ^2A_n, we can consider the $(n + 1)$th 2-RDM as a function of ϵ_n as it approaches 0 from the positive direction:

$$^2D_{n+1}^{pq;st}(0^+) = \lim_{\epsilon_n\to 0^+}{}^2D_{n+1}^{pq;st}(\epsilon_n) \quad (11)$$

$$= {}^2D_n^{pq;st}(\epsilon_{n-1})$$
$$+ \lim_{\epsilon_n\to 0^+}\epsilon_n\langle\Psi_n|[a_p^\dagger a_q^\dagger a_t a_s, {}^2\hat{A}_n]|\Psi_n\rangle. \quad (12)$$

While this quantity theoretically approaches $^2D_n(\epsilon_{n-1})$ as $\epsilon_n \to 0^+$, in practice the discrete unitary gates are subject to substantial noise on current-to-intermediate-term quantum computers and, hence, do not collapse to the identity operator for any actual gate sequence. The noise channels in general
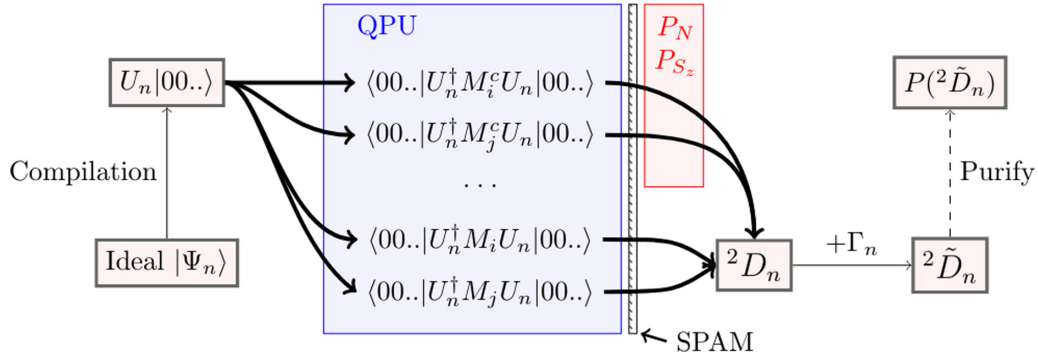
FIG. 2. Error-mitigation scheme to obtain corrected 2-RDMs. We first take a set of instructions, and construct the appropriate circuit design. We run these on the quantum computer to obtain a set of measurement results which are then corrected through the inversion of a state preparation matrix (SPAM, small hatched rectangle). Measurements corresponding to diagonal elements of the 2-RDM (M_i^c) will commute with the $\hat{N}$ and $\hat{S}_z$ symmetries, and so are projected onto the proper operator space. We then apply our shift correction, Γ_n, which also preserves trace but can introduce negative eigenvalues, and optionally, a purification of the 2-RDM.

will contract the set of possible 2-RDMs (e.g., for systems with strong depolarizing errors this is to a fully depolarized 2-RDM). For our system, this can lead to a result that any energy obtained will be higher than the energy of the previous step (see Appendix C 3 for an example). In these instances, the change in energy due to noise is greater than any change from the optimization.

Let $^2\Gamma_n$ be a matrix of the same rank as the 2-RDM, and $^2\tilde{D}_n(\epsilon_n)$ be the corrected 2-RDM. Then, we define a correction by the following system of equations:

$$^2\tilde{D}_{n+1}(\epsilon_n) = {}^2D_{n+1}(\epsilon_n) + \sum_{i=0}^{n} {}^2\Gamma_i, \qquad (13)$$

$$^2\Gamma_n = {}^2D_n(\epsilon_{n-1}) - {}^2D_{n+1}(0^+), \qquad (14)$$

$$^2D_0 = {}^2D_{\text{HF}}. \qquad (15)$$

Equation (13) defines the error-mitigated 2-RDM at each step. The $^2\Gamma_n$ in Eq. (14) is the difference between the new state with $\epsilon_n = 0^+$ and the previous state. Equation (15) gives the initial condition of the system. The correction helps to avoid noise-related barriers in the optimization surface [as $^2\tilde{D}_{n+1}(0^+) = {}^2D_n(\epsilon_{n-1})$], allowing us to reach 2-RDMs that are normally inaccessible due to the noise. For a noise-free simulation, we also have that $^2\Gamma_n = 0$ for all n, ensuring that we would maintain the exact result on a perfect quantum computer. We use the corrected 2-RDM $^2\tilde{D}_{n+1}$ throughout the optimization in evaluating the energy as well as choosing the elements of $^2A_{n+1}$. While the gradient information reflected in ^2A around ^2D and $^2\tilde{D}$ will not be the same when $^2\Gamma$ is large, because we are optimizing $E[^2\tilde{D}_n]$, and because we generate ^2A_n with Eq. (8), this is the appropriate choice. If we were to use Eq. (10) instead, then we would obtain information around ^2D_n, and would have to correct ^2A as well.

There are a number of practical considerations in the implementation of the $^2\Gamma$ correction such as the potential variability of the noise. Because we are adding RDMs with separate uncertainties, the uncertainty in the result increases (if we assumed independent $^2\Gamma_i$ with equal standard deviations σ, this would be $\sqrt{n}\sigma$ after n iterations), which may require us to increase the sampling of $^2\Gamma_i$. The errors affecting the quantum computer may exhibit a time dependence on the

order of the run time. To avoid this possibility, we run the results as contiguously as possible with the total number of iterations n being kept relatively low (for all instances $n \leqslant 6$). Additionally, the 2-RDM is purified in some cases to ensure that the negative eigenvalues of the 2-RDM and the related two-hole and particle-hole RDMs (see next section) are eliminated. Regardless, we find this error-mitigation strategy to be necessary to obtain meaningful results within the context of an iterative *Ansatz*.

D. Purification of the 2-RDM

As mentioned above, the effect of noise in a quantum simulation is that the measured quantum state might no longer represent a physical system. While we cannot directly assess the purity or fidelity of an RDM, we can "purify" the 2-RDM to ensure that the eigenvalues of the various permutations of the particle- and hole-reduced density matrices are positive semidefinite, which are necessary criteria for a pure-state or ensemble N-representable 2-RDM [65]. A matrix is positive semidefinite if and only if its eigenvalues are non-negative. For instance, for the 2-RDM, the two-particle (^2D), two-hole (^2Q), and particle-hole (^2G) matrices must have non-negative probabilities and, hence, must be positive semidefinite in a set of conditions known as the 2-positivity (or DQG) conditions [59,66–68]

$$^2D \succcurlyeq 0, \qquad (16)$$

$$^2Q \succcurlyeq 0, \qquad (17)$$

$$^2G \succcurlyeq 0, \qquad (18)$$

where the elements of these metric matrices are given by

$$^2D_{kl}^{ij} = \langle\Psi|\hat{a}_i^\dagger\hat{a}_j^\dagger\hat{a}_l\hat{a}_k|\Psi\rangle, \qquad (19)$$

$$^2Q_{ij}^{kl} = \langle\Psi|\hat{a}_k\hat{a}_l\hat{a}_j^\dagger\hat{a}_i^\dagger|\Psi\rangle, \qquad (20)$$

$$^2G_{kj}^{il} = \langle\Psi|\hat{a}_i^\dagger\hat{a}_l\hat{a}_j^\dagger\hat{a}_k|\Psi\rangle. \qquad (21)$$

We accomplish the purification by semidefinite programming, which allows us to minimize an function of a matrix subject to linear constraints while ensuring that the matrix remains
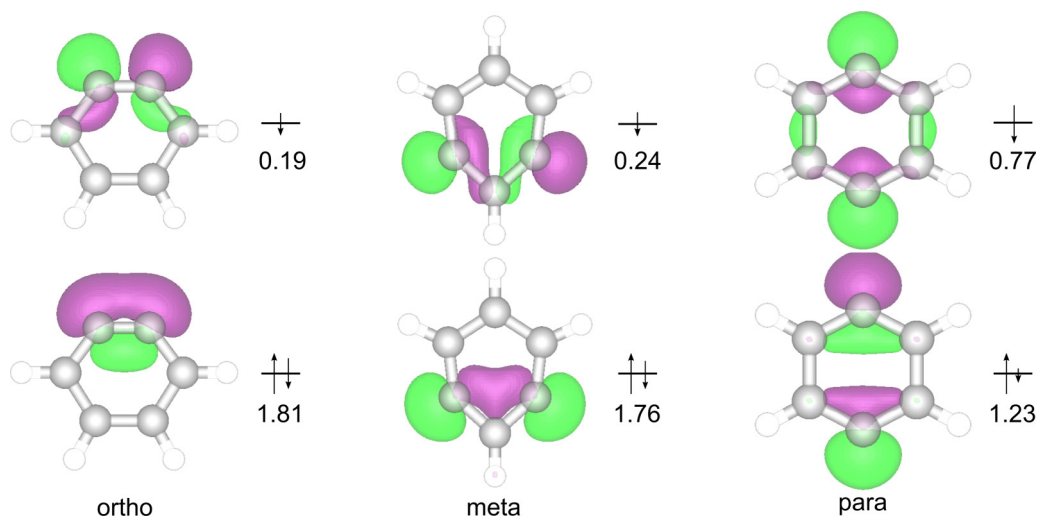
FIG. 3. Molecular-orbital diagram and natural-orbital occupations of the highest and occupied lowest natural orbitals for ortho-, meta-, and para-benzyne. Geometries for the ortho- and meta- isomers were obtained from [80] and optimized with spin-flip time-dependent density functional theory (SF-TDDFT), and the para-isomer was obtained from [81] and optimized with spin-flip coupled cluster with singles and doubles (SF-CCSD).

positive semidefinite [69–71]. The general method was developed by one of the authors for reconstructing noisy processes for quantum tomography [59], and was more recently applied in the context of quantum simulation by Rubin *et al.* [60].

The objective in this work is to create a purified 2-RDM, $^2D_{SDP}$, which minimizes the norm of the error matrix $E = {}^2D - {}^2D_{SDP}$, subject to the DQG constraints ensuring that $^2D_{SDP}$ represents a physical system. To express this as a semidefinite program, we take F to be a matrix of free variables, and then minimize the trace of the following block matrix:

$$\begin{pmatrix} I & E \\ E^\dagger & F \end{pmatrix} \succcurlyeq 0. \tag{22}$$

Taking the determinant of the 2×2 block matrix allows us to relate the trace of F to the Frobenius norm, providing a semidefinite relaxation for the minimization problem. The DQG constraints can be expressed in a block-diagonal form

$$\begin{pmatrix} {}^2D & 0 & 0 \\ 0 & {}^2Q & 0 \\ 0 & 0 & {}^2G \end{pmatrix} \succcurlyeq 0. \tag{23}$$

These semidefinite conditions, the linear mappings between the metric matrices, and the trace of the 2-RDM define the constraints in the SDP. To solve the SDP, we use a boundary-point algorithm for the direct variational calculation of the 2-RDM [71–74]. The algorithm for purification of the 2-RDM with the DQG conditions has a scaling of $O(r^6)$.

III. BENZYNE CALCULATIONS

In this work we use the QACSE method to investigate the *ortho-*, *meta-*, and *para*-isomers of benzyne, which may be obtained via the elimination of two substituents in the relevant positions of the benzene ring. Owing to their versatility as reactive intermediates in biological processes, derivatives of the isomeric benzynes have been the subject of a growing in-

terest in the synthetic research community in the development of biomimetic reactions [75], such as the Diels-Alder reaction [76] and in so-called "click chemistry" [77], with a wide range of applications to the synthesis of heterocycles [78] and natural products [76]. Even though biradicals such as benzyne play key roles across synthetic and materials chemistry, making their accurate theoretical description quintessential to the understanding of chemical processes, their exact treatment continues to pose a challenge to electronic structure theory [53,54]. Details regarding the electronic structure treatment of these systems are included in Appendix A.

Figure 3 shows the structures for each of the three isomers, as well as the occupations of the highest and lowest occupied natural orbitals. The energetic ordering of the three isomers follows their degree of diradical character, with experimental gas phase heats of formation showing ortho-isomer as the energetically lowest isomer, followed by the meta- and then para-isomers, at energies of 10 ± 3 kcal/mol and 22 ± 3/kcal/mol relative to the ortho reference, respectively [79]. The variations in ground-state energy and diradical character are driven by the degree to which the geometric constraints of the given isomer allow for overlap between the singly occupied carbon-p orbitals, which is demonstrated by the electron densities of the highest occupied natural orbital (HONO) and the lowest unoccupied natural orbital (LUNO), shown in Fig. 3. In the ortho-isomer, adjacency of the singly occupied orbitals allows for good overlap and energetically favorable formation of a bond with significant π character, giving this isomer C-C triple bond character. While somewhat compensated by geometric distortion, driven by the greater C-C radical distance the magnitude of this bonding interaction is reduced in the meta-isomer, and essentially diminished in the para geometry, where no overlap between the lobes of the carbon-based radical orbitals is geometrically feasible.

Aside from the relative ground-state energies, the singlet-triplet gaps of these isomers are well documented experimentally and are used for benchmarking multireference electronic

TABLE I. Relative energies between the configurations of ben-zyne with classical CASSCF and QACSE methods for differing active spaces and levels of error mitigation, in kcal/mol. [0,0] active space refers to the initial Hartree-Fock calculation. M refers to a state preparation and measurement error, P to the application of the number projection, L to the use of the $^2\Gamma_n$ correction, and $+$ to the SDP corrected state.

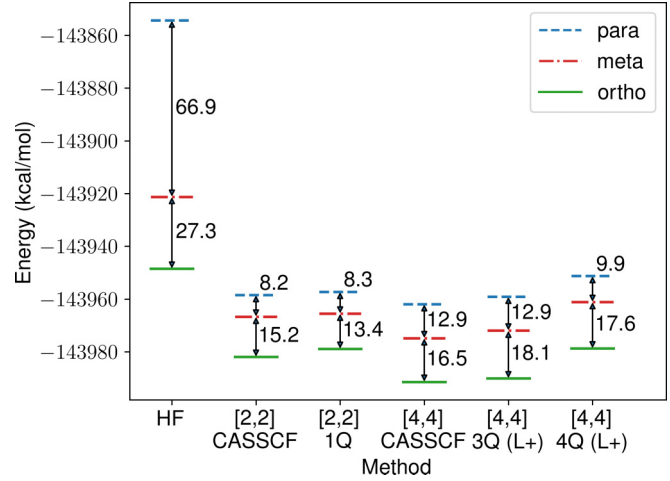| Method	[X,Y]	Number qubits	Error mitigation	$E_{\text{isomer}} - E_{\text{ortho}}$ (kcal/mol) meta	para
CASSCF	[0,0]			27.3	94.2
	[2,2]			15.2	23.4
	[4,4]			16.5	29.5
QACSE	[2,2]	1	M	13.4	21.7
	[4,4]	3	MP	19.6	15.4
	[4,4]	3	MPL	32.5	55.7
	[4,4]	3	MPL+	18.1	31.0
	[4,4]	4	MPL	27.1	23.6
	[4,4]	4	MPL+	17.6	27.5
Expt. [79]				10 ± 3	22 ± 3

FIG. 4. Overview of results shows active space calculations for the different configurations of benzyne across several methods, including Hartree-Fock, CASSCF, and QACSE for [2,2] and [4,4] active spaces. The three- and four-qubit results utilize the limit-preserving correction (L) and purification ($+$) schemes of error mitigation. The data correspond with results taken in Table I.

structure methods [53,54,57]. In this work we focus on resolving the differing degrees of correlation present solely in the ground-state 2-RDMs. As the radical electrons are localized in orbitals perpendicular to the π system, a minimal [2,2] active space is sufficient to describe the multireference correlation in these systems and the inclusion of additional orbitals solely results in the recovery of additional dynamic correlation. A recently published companion work utilizes these results as the kernel for a classical calculation that includes dynamic correlation effects from orbitals beyond the active space [82]. The inclusion of these orbitals as well as larger basis sets is necessary for more rigorous experimental comparisons. An exploration of the singlet-triplet gaps is the goal of future work.

The relative energies from the complete active space self-consistent field method (CASSCF) and from the quantum calculations are listed in Table I and Fig. 4 for the [2,2] and [4,4] active spaces where the notation [X,Y] denotes X electrons in Y orbitals. The CASSCF calculations optimize the active electrons and orbitals in the mean field of the remaining electrons and orbitals. The target CASSCF results yield the correct ordering, although each gap is slightly higher than experimental values. For the [2,2] case, the meta and para energies relative to ortho are 15 and 23 kcal/mol, respectively. For the [4,4] active space, the meta and para energies relative to the ortho configuration are 13 and 29 kcal/mol, respectively. The [2,2] active space corresponds with a one-qubit quantum calculation, whereas the [4,4] calculation was performed with four and three qubits, representing exact and near-exact symmetries, respectively (see Appendices B 2, B 1, and B 3). The error mitigation ranges from a simple measurement correction to our full scheme of corrections (denoted $L+$, or MPL+). M refers to a state preparation and measurement, P to the application of the number projection, L to the use of the $^2\Gamma$ correction, and $+$ to the SDP corrected state. The error in the obtained relative energies on the quantum

computer in the [4,4] case is 1.6 kcal/mol (2.6 mhartree) for both the three-qubit (3Q) and four-qubit (4Q) cases, whereas for the [2,2] space, we obtain a result within 2 kcal/mol (3 mhartree). The number of unique iterations is between 3 and 6, depending on the *Ansatz* developed. The operators in the qubit basis (see Appendix B 6) for the three-qubit calculations have 0–8 controlled NOT (CNOT) gates, while the pool of operators for the four-qubit operators each have 8–12 CNOT gates.

Another comparison between the error-mitigation schemes is seen in the target energies for each calculation relative to the classical CASSCF result. These errors are listed in Table II. In particular, despite having differences between configurations of only a few kcal/mol, the difference from the CASSCF results for results without the $^2\Gamma$ correction is around 20 to 30 kcal/mol higher than the target energies across the configurations. These results are more common for what might be expected from noisy quantum devices, as often the lowest-energy states are not the final state of the optimization. The $^2\Gamma$-corrected results on the other hand in some instances can

TABLE II. Difference in energy between the QACSE methods including various error-mitigation schemes and the CASSCF result in millihartrees (mhartree).

[X,Y]	Number qubits	Error mitigation	Error relative to CASSCF (mhartree) ortho	meta	para
[2,2]	1	M	4.8	1.9	1.9
[4,4]	3	MP	51.9	43.2	29.5
[4,4]	3	MPL	−53.6	−28.1	−11.8
[4,4]	3	MPL+	2.1	4.6	4.5
[4,4]	4	MPL	−25.9	−9.0	−35.3
[4,4]	4	MPL+	20.2	21.9	17.0

TABLE III. Largest natural-orbital occupation numbers for the CASSCF results and the purified, $^2\Gamma$-corrected results for the [2,2] and [4,4] active spaces on the quantum computer. In each case, the para-benzyne solution exhibits biradical character in the highest occupied and lowest unoccupied natural orbitals, though to differing degrees based on the method.

Method	[X,Y]	Number qubits	Orbital	Orbital occupations ortho	meta	para
CASSCF	[2,2]		HONO	1.811	1.712	1.232
	[2,2]		LUNO	0.189	0.288	0.768
QACSE	[2,2]	1	HONO	1.695	1.604	1.127
	[2,2]	1	LUNO	0.305	0.396	0.873
CASSCF	[4,4]		HONO − 1	1.947	1.977	1.981
	[4,4]		HONO	1.813	1.756	1.235
	[4,4]		LUNO	0.187	0.244	0.765
	[4,4]		LUNO + 1	0.053	0.023	0.019
QACSE	[4,4]	3	HONO − 1	1.956	1.976	1.992
	[4,4]	3	HONO	1.851	1.761	1.148
	[4,4]	3	LUNO	0.149	0.239	0.852
	[4,4]	3	LUNO + 1	0.045	0.012	0.008
QACSE	[4,4]	4	HONO − 1	1.973	1.985	1.956
	[4,4]	4	HONO	1.938	1.570	1.200
	[4,4]	4	LUNO	0.054	0.433	0.790
	[4,4]	4	LUNO + 1	0.036	0.012	0.055

be below the variational CI bound, highlighting the need for purification. Comparisons with ideal results in Appendix B 5 show that the ideal QACSE essentially achieves the CASSCF result, while the ideal reconstructed 3-RDM-based approach yields errors on the order of millihartrees with the largest error for meta-benzyne. While the error from the reconstruction might seem significant, it is an order of magnitude smaller than the error from the noise on the quantum devices..

Finally, the natural-orbital occupation numbers, which are the eigenvalues of the 1-RDM, can help infer the nature and degree of electron correlation in the system. The Hartree-Fock state, corresponding with a single determinant, has eigenvalues of 2 or 0 across all (spatial) orbitals, while a biradical system would exhibit equal occupations of 1 in the highest occupied and lowest unoccupied natural orbitals. We report the natural orbital occupations for the CASSCF and purified results in Table III for the one-, three-, and four-qubit QACSE calculations. In each case, we see significant differences between the para-isomer and the other two isomers (ortho and meta) on the quantum computer. The para-benzene, which does not have any overlapping density between the carbon p orbitals (see Fig. 3), exhibits biradical character, whereas the other two configurations exhibit more single-reference character. This is also reflected in the amount of correlation energy recovered ($E_{\mathrm{CASSCF}} - E_{\mathrm{HF}}$) for each configuration (see Fig. 4). When compared to the CASSCF occupations, the results for the three-qubit case were all within 0.09 of the target occupations. In the four-qubit case the ortho (0.14) and meta (0.19) HONO and LUNO occupations have more significant errors, which could be expected from the increased absolute energies seen for each of these isomers. By looking at the HONO−1 and LUNO+1 orbitals in the [4,4] space,

we also see that the fractional occupations of the HONO and LUNO are not an artifact of error on the quantum computer, as the closeness of the HONO−1 and LUNO+1 occupations to 2 and 0 is maintained.

IV. DISCUSSION

The results of these benzyne calculations highlight the potential for quantum simulation on near-term devices, particularly with quantum RDM methods and error-mitigation tools designed for RDMs. Although work in our group and elsewhere has investigated and obtained highly accurate results for small systems or particular configurations of electrons (namely, in taking advantage of pure N-representability constraints) [4,20,83], this work represents a step towards more general quantum computing algorithms based on RDM theory. Indeed, the [4,4] active space represents an important step from model systems and minimal cases towards the end goal of robustly treating strongly correlated many-body systems. These results also demonstrate a useful classical-quantum hybrid approach, incorporating elements from both classical and quantum techniques.

With regards to the number of iterations and the variational cost, for many systems, including the benzyne isomers, the QACSE method is consistently able to recover a large part of the correlation energy within a few iterations. While we also evaluated derivative-free one-dimensional optimizers that might be able to help in a noisy landscape [14,20,39], practically, the trust-region optimization combined with a rejection criteria provides a reliable way of choosing a step size for Eq. (4), and making sure that convergence progresses as a whole. The rejection criteria in particular eliminate iterations which do not contribute to the *Ansatz* properly with an optional reevaluation of the last ^2A_n step. This helps in particular with overcoming instances where the errors in the gradient are too large to take a meaningful step. It is also worth mentioning that the experimental requirements for convergence and termination of the method are different from ideal conditions. While lowering the residuals of the ACSE is ideal, and ensures a properly converged state, noise will decrease the likelihood of reaching a meaningful RDM. Because of the limitations of noise, in the present multiqubit examples the ^2A matrix is updated by a classical algorithm with reconstruction of the 3-RDM rather than the quantum algorithm shown in Eq. (10). In these instances, error from reconstruction of the 3-RDM is lower than the error from the noise on the quantum devices. Importantly, the classical and quantum algorithms can be interchanged depending upon the complexity of the circuit and the level of noise on a given device.

These results highlight the necessity of different error-mitigation schemes. The qubit reduction technique allows for significant simplification of the problem (although not to a trivial degree for the [4,4] case), as well as different thresholds of accuracy. It is somewhat known that with the Jordan-Wigner transformation and r spatial orbitals, for molecular systems one can always find two Z symmetries of length r, corresponding to the constant parity of the α and β sets of orbitals in a N- and S_z-preserving simulation, which reduces the number of qubits to $2r - 2$ (similar to ideas covered elsewhere [3,84]). Applying additional symmetries from the

Hamiltonian is exact, with the limitation that the final and initial states share the same symmetries. For systems with near symmetries (symmetries existing in a modified Hamiltonian), elimination of small nonzero elements can help to find these symmetries (see Appendix B 3). In general, further tapering of a state to a symmetry that does not exactly commute with the Hamiltonian will constrain the state space, yielding an approximation to the eigenstate.

To further motivate this, we can consider the symmetry constrained state as an approximation to the full state. Within quantum chemistry numerous approximations are commonly made based on available computational resources, such as the use of finite basis sets, the separation of nuclear and electronic motion, and the truncation of the manifold of excitations [9]. On a quantum computer a significant consideration is the level of noise generated in a preparation and measurement from the complexity of the circuits. In the context of NISQ systems, a theoretically lower-quality *Ansatz* can produce a better result than a higher-quality, or even exact, *Ansatz* if the added noise offsets the improvement in accuracy from the theoretically superior *Ansatz*. Additionally, the combination of noise and error-mitigation techniques can result in 2-RDMs whose energies are below those from noiseless simulations but above those from an exact calculation in the given basis set. For these reasons, it is not surprising that the three-qubit case can produce results that are superior to the four-qubit case with approximate symmetries.

We did not explicitly identify the effect of the measurement errors involving the inversion of the state transition matrix, although these have been documented elsewhere to help improve results on the order of the measurement error. Because incorrectly measured states can easily lead to different particle states, this can lead to large differences in the obtained energies. However, regardless of the measurement error, the projection of the RDM onto the correct particle number space in the diagonal entries is a critical step. The energetic effect of this correction is system dependent, but can easily be on the order of hartrees. Quite simply put, the results are often not meaningful without this correction, which can also be seen in its success in other work [4,83]. While it is preferable in theory to correct the diagonal and off-diagonal elements of the 2-RDM, for the latter instances, a measurement sequence which commutes with the particle-number operator must be developed. Additionally, this greatly changes the tomography requirements of the 2-RDM, rendering useless the advantages of local measurement commutation. The incremental improvements in the quantum devices over the last few years are also critically important, as other devices were tested that did not achieve the same level of results (not reported).

The $^2\Gamma$ correction serves indirectly to expand the set of accessible 2-RDMs while preserving the integrity of the iterative optimization. While the application here to an iterative *Ansatz* is unique, the idea at each iteration could be seen as a zeroth-order extrapolative procedure, like the Richardson extrapolation, repeated at each iteration [17,85]. Instead of attempting a linear or higher-order fit to a variable noise strength, we simply add a correction RDM. As a result, we do not have to deal with adjusting how noise is applied in the underlying pulse, and the cost of the mitigation procedure is

kept low. Even if at each step we recalculated $^2\Gamma$, the number of evaluations would be linear with respect to n. While the implementation here is straightforward, it is likely that this method or variations on it could be applied to other iterative methods in a straightforward manner. In terms of the set of possible RDMs that can be measured, this approach slowly shifts our corrected RDM by $^2\Gamma$ through the set of all possible RDMs. Qualitatively, the effect of this strategy on the obtained benzyne energies is to improve the result usually by tens of mhartrees, and in some instances up to 0.1 Hartree. However, as it is possible to move beyond the boundary of the set of physical RDMs, purification of the RDM is a necessary step, albeit with approximate *N*-representability conditions. The distance between the $^2\Gamma$-corrected 2-RDM and the purified 2-RDM, can be used as an exclusionary criterion in the optimization.

Both QACSE and ADAPT-VQE use the ACSE wavefunction *Ansatz* [31–34] that was developed in the ACSE literature [33–36] (for example, see Sec. II E of Ref. [34]). The structure of this wave function, a product of unitary two-body exponential operators on a reference wave function, has the ACSE as its stationary equation [31,34]. The ACSE *Ansatz* is related to the single-term two-body exponential *Ansätze* [86–93] and the two-body exponential product *Ansätze* [31,32], which were investigated in the context of the contracted Schrödinger equation (CSE) [23–30]. Notably, while this wave function has been stated heuristically and called an adaptive generalized unitary coupled-cluster singles and doubles wave function in the ADAPT-VQE literature, its stationary equation is not a coupled-cluster equation, and its definition in the ACSE literature significantly predates its recent discussion. In fact, Grimsley *et al.* [52] describe ADAPT-VQE as "not so much an approximation to UCC (unitary coupled cluster) as it is a wholly unique *Ansatz*. From this perspective, by minimizing the ACSE wave function, both QACSE and ADAPT-VQE are seeking solutions of the ACSE, rather than a direct solution of the Schrödinger equation as in VQE, and, hence, both can be understood as types of contracted quantum eigensolvers. The distinction between the VQE and CQE is important because the CQE framework informs both the structure of the wave function and its stationary condition.

Although both QACSE and ADAPT-VQE can be viewed as quantum solutions of the ACSE, their motivations and initial implementations have significant differences. Unlike the ADAPT-VQE which optimizes all parameters in the wave function simultaneously in the spirit of the variational principle of the wave function governing VQE, the ACSE takes a greedy, iterative approach in which the wave function is optimized only with respect to the two-body exponential transformation of the current iteration. This more targeted optimization leads to a contracted stationary condition, the solution of the ACSE, which is a hallmark of the ACSE theory [31–34].

Specifically, the ADAPT-VQE [52] defines a predefined pool of parametrized unitary two-body exponential operators from which the ACSE wave function can potentially be constructed from the reference (Hartree-Fock) wave function. The algorithm improves the trial ACSE wave function at the nth iteration by (i) multiplying the $(n - 1)$th ACSE wave function

by the operator from the pool with the largest energy gradient and (ii) reoptimizing the energy with respect to all parameters in the pool operators. In contrast, the QACSE does not use a predefined pool of operators but rather computes the residual of the ACSE either from an efficient quantum measurement of an effective 2-RDM as shown in Eq. (10) or a classical evaluation where the 3-RDM is approximately reconstructed. This generality gives the QACSE additional flexibility, which may become increasingly important in the treatment of larger, more correlated atoms and molecules where a limited operator pool may miss significant correlation effects. Perhaps most importantly, because the QACSE is aiming to satisfy the ACSE rather than the standard variational principle for the wave function, the QACSE does not reoptimize its parameters in previous steps as in part (ii) of the ADAPT-VQE algorithm. While a reoptimization phase decreases circuit depth, especially for small molecules, it is not necessary for converging to a solution of the ACSE, and it may require a significantly larger number of energy function and gradient evaluations for larger molecules.

V. CONCLUSIONS

Molecular simulations on quantum computers have the potential to treat strongly correlated problems that are currently intractable on conventional computers. The practical realization of such simulations, however, requires quantum molecular algorithms that are mappable to transformations, such as products of unitary transformations, that are natural for quantum computers. Here we implement a contracted quantum eigensolver (CQE) from a contraction of the Schrödinger equation onto the space of only two electrons, known as the anti-Hermitian contracted Schrödinger equation (ACSE). To make the solution of the ACSE more practical for more realistic chemical problems on quantum computers, we utilize robust error-mitigation techniques, including techniques based on N-representability constraints. The solution of the anti-Hermitian CSE (ACSE) through iterative minimization of its residual generates a rapidly convergent product of two-body unitary transformations that is natural for implementation on quantum computers. Furthermore, unlike the solution of the ACSE on the classical computer, the contracted Schrödinger solver on quantum computers can fully or partially remove approximate reconstructions of higher RDMs and, hence, can potentially achieve exact results without the exponential complexity of the many-electron wave function.

The combination of the ACSE solver with robust error mitigation provides a scalable approach to molecular simulations on quantum computers with low circuit depth and few variational parameters. We apply the algorithm to the resolution of the *ortho*-, *meta*-, and *para*-isomers of benzyne C_6H_4. The relative energies exhibit single-digit millihartree errors, and the computed natural-orbital occupations capture the biradical nature of the *para*-isomer. The molecular simulation of the benzyne isomers represents an important step in eigensolver and error-mitigation technologies towards the practical simulation of larger, even more complex molecules on quantum computers.

APPENDIX A: ELECTRONIC STRUCTURE CALCULATION

Complete active state self-consistent field (CASSCF) calculations were performed as implemented in the Maple Quantum Chemistry Package [94–96] using [2,2] and [4,4] active spaces with the correlation-consistent valence double-zeta (cc-pVDZ) basis set [97]. Following convergence of the CASSCF procedure, effective active space electron integrals for the quantum ACSE calculation were obtained via the folding of the core-active cross terms into the active space, such that the effective active space energy is given by

$$\tilde{E}_{act} = \frac{1}{2} \sum_{pqst} {}^2\tilde{K}_{st}^{pq}\, {}^2D_{st}^{pq}, \tag{A1}$$

where ${}^2\tilde{K}_{st}^{pq}$ are the active space electron integrals containing the core-active cross terms. The elements of the effective active space integral matrix ${}^2\tilde{K}_{st}^{pq}$ are constructed from the one- and two-electron integrals as follows:

$$ {}^2\tilde{K}_{st}^{pq} = \frac{1}{N-1}\big({}^1\tilde{K}_s^p \delta_t^q + {}^1\tilde{K}_t^q \delta_s^p \big) + {}^2K_{st}^{pq}, \tag{A2}$$

where

$$ {}^1\tilde{K}_s^p = {}^1K_s^p + \sum_i \big(2\, {}^2K_{si}^{pi} - {}^2K_{is}^{pi} \big), \tag{A3}$$

and p, q, s, t runs over all active orbitals and i runs over all core orbitals.

While we could also include number-excitation terms, because we start with a multireference guess solution, the number-excitation terms are small, even after a few iterations, and can be mostly ignored. Using solely double excitations allows for sufficient quality results convergence. Part of the difficulty in describing the meta-benzyne configuration is that the solution could be described as more single reference, and requires more than a few excitation terms with small coefficients to be described properly.

APPENDIX B: QUANTUM CALCULATION

Using the electron integrals for the active space from above, we perform a quantum calculation on different IBMQ devices. In particular, we perform [2,2] and [4,4] calculations under the Jordan-Wigner transformation. Different IBMQ devices were utilized through the IBM Quantum Experience. These devices utilize fixed-frequency transmon qubits with coplanar waveguide resonators [98,99]. We use the PYTHON 3 package QISKIT (v 0.15.0) [100] to interface with the device. The calculations themselves are multifaceted, with nonstandard approaches taken in a number of different areas. We

document these in subsequent sections. Each measurement was performed with 2^{13} shots. Stochastic effects were on the order of mhartree, though are affected in a substantial way through the purification scheme. For the collection of all 2-RDMs we utilized a symmetry-projected operator basis using the $\hat{N}$ and $\hat{S}_z$ symmetries [101].

For the one-qubit calculations, we utilized IBMQ-Rome, while for the three- and four-qubit calculations, we utilized IBMQ-Bogota and IBMQ-Santiago. QISKIT was used to interface with the IBMQ devices.

1. Quantum [2,2] active space calculations

Using the Jordan-Wigner transformation, the [2,2] case with four spin orbitals maps to four qubits. The [2,2] calculations contain two Pauli symmetries related to the parities of the total number of electrons and the number of electrons in a subset of spin orbitals (either α or β), and a further symmetry is found for most molecular systems, allowing the [2,2] system to be represented with a single qubit. These can be expressed as

$$S_1 = \{Z_1 Z_2, Z_1 Z_3, Z_1 Z_4\}. \tag{B1}$$

The elements of ^2A were determined through the quantum ACSE method, with Euler's method being used to propagate the *Ansatz*. An l_2 norm of ^2A below 0.01 was used as the stopping criterion, which was usually reached in 10–12 iterations. The exact exponential of any combination of Pauli operators is well known for the single-qubit case, and so we are able to exactly express $U = \prod_i e^{A_i}$ as well as $U' = e^{iH\delta} \prod_i e^{A_i}$. For these runs, we chose $\delta = 0.25$.

2. Quantum [4,4] active space calculations

The Jordan-Wigner representation maps the [4,4] case with eight spin orbitals to eight qubits. Again, two symmetries related to fermionic parity can be utilized, and then depending on the Hamiltonian we can find additional symmetries. For these particular integrals, we find two additional symmetries across all configurations, and then an additional symmetry for the para-configurations, which can be applied to the ortho- and meta-configurations as approximate symmetries. A more detailed discussion on the process of finding these symmetries is included in the next section. While we can also find approximate symmetries through truncation of the Hamiltonian, the application of this additional symmetry from the para-isomer yielded sufficient results for the ortho-isomer case, with a difference from the target (CASSCF) energy of 9.2×10^{-4} H. For the meta case, we found an additional symmetry with approximately 0.6×10^{-3} H error from the CASSCF. The solutions are exact for the three-qubit para, and all of the four-qubit cases. We show the effects of some approximate tapering schemes in the next section.

The symmetries are listed in the following set for the four- and five-symmetry cases, respectively:

$$S_4 = \{Z_1 Z_2 Z_3 Z_4, Z_1 Z_2 Z_5 Z_6, Z_1 Z_3 Z_5 Z_6, Z_2 Z_3 Z_5 Z_8\}, \tag{B2}$$

$$S_3^{p/q} = \{Z_1 Z_2 Z_3 Z_4, Z_1 Z_5, Z_2 Z_6, Z_3 Z_7, Z_1 Z_2 Z_3 Z_8\}, \tag{B3}$$

$$S_3^m = \{Z_1 Z_4, Z_2 Z_3, Z_1 Z_2 Z_5 Z_6, Z_1 Z_2 Z_5 Z_7, Z_5 Z_8\}. \tag{B4}$$

As a result, we are able to perform three- and four-qubit simulations of these systems on the five-qubit linearly connected IBMQ-Bogota device, and IBMQ-Santiago. When tapering off qubits, we use eigenvalues which match the eigenvalues of the initial Hartree-Fock determinant. While the initial determinant in this paper is consistently a closed-shell configuration, it can also represent an open-shell configuration for an extension of the procedure to open-shell systems.

The calculations themselves utilized a one-dimensional model trust-region Newton's method, where the initial trust region was taken to be 2, and the quadratic fit was taken from $\epsilon_n = \pm 1$. Additionally, we used a threshold of $0.75 \times a_{\max}$ where $a_{\max}$ indicated the largest magnitude term in the ^2A for a given iteration. The convergence criteria were taken to be 0.02–0.03 in the trust-region criteria (or in the norm of ^2A), and we used five-to-six iterations. Instances of the runs themselves are included in the open-source HQCA software package [102].

3. Qubit reduction by tapering and Hamiltonian truncation

The qubit-reduction scheme follows previous work by Bravyi *et al.* and expanded by Setia *et al.* for applications to point-group symmetries [84,103]. In particular, we express the Hamiltonian in the Pauli basis and then put these terms in a check sum representation to construct the generator and parity check matrices from the field of quantum error correction [104]. By performing Gaussian elimination on the parity check matrix, we can find generators of the Hamiltonian, which in turn allow us to select a basis for the corresponding null space. Elements of the null space will commute with every term in the Hamiltonian, and thus are symmetries of H. Thus, the nullity of this matrix is the number of symmetry elements, and thus the number of qubits which we can taper. By using a particular unitary transformation

$$U_i = \frac{1}{\sqrt{2}}(X_j + s_i), \tag{B5}$$

where X_j is selected so that X_j anticommutes with s_i, and commutes with all other s_i, $1 \neq j$, we transform the Hamiltonian so that qubits j have only X or I in each term. By selecting an appropriate eigenvalue of X, we can taper off these terms, resulting in a modified fermionic transformation. We use eigenvalues which agree with the eigenvalues of the initial closed-shell singlet Hartree-Fock determinant.

For a general $\hat{N}$- and $\hat{S}_z$-preserving state, there exist two symmetries related to the parities of the α or β electrons. One can see this simply by noting that there exist two Pauli strings of length r, over the α and β electrons, respectively, which can be selected. These symmetries preserve the commuting and anticommuting relations described in Bravyi *et al.* [84] and, hence, can be tapered as symmetries of the Hamiltonian (or more generally, the set of all 2-RDM operators). While mappings such as the parity or Bravyi-Kitaev mapping explicitly assign these symmetries to qubits, we still can identify and utilize these symmetries with the Jordan-Wigner transformation.

As mentioned in the Discussion section, we can exploit approximate symmetries for a decrease in circuit complexity by either projecting the state onto a nearby symmetry or truncating the Hamiltonian. To show the effect of using
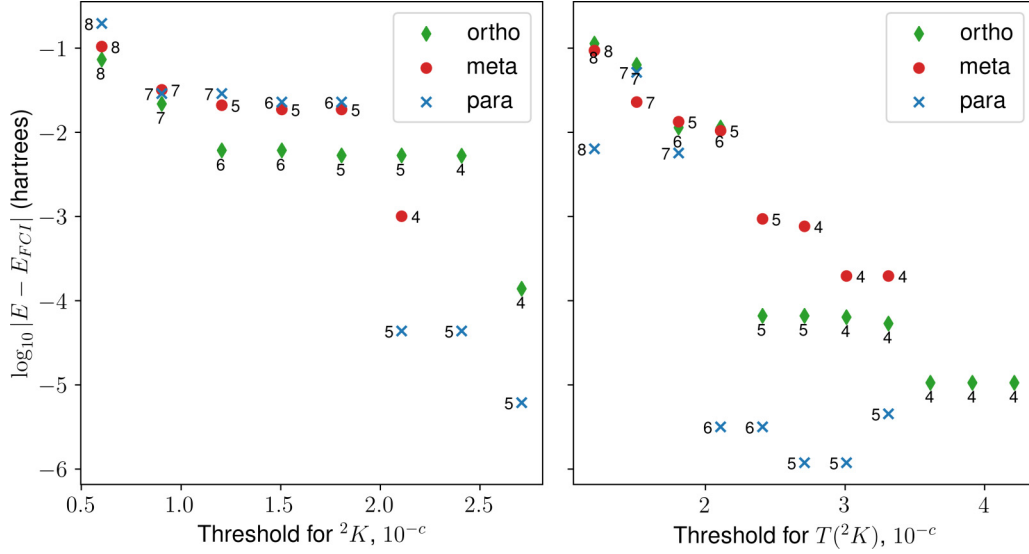
FIG. 5. Comparison of the lowest energy following truncation of the reduced Hamiltonian ^2K matrix (left) and the transformed set of Pauli operators $T(^2K)$ (right) for ortho-, meta-, and para-benzyne, with respect to the CASSCF results. The number of symmetries found (i.e. the nullity of the generator) is reported below, to the right, and to the left of the marker for the ortho-, meta- and para-benzyne isomers respectively.

approximate symmetries through tapering Hamiltonian elements, Fig. 5 shows the accuracy and potential symmetries that can be found for a given truncation of elements of either the reduced Hamiltonian or the transformed Hamiltonian in the Pauli string basis. In particular, we are interested in finding the highest-symmetry state, the state whose generator matrix has the largest null space that is consistent with energy errors below a given threshold. For these instances, the ortho-, meta-, and para-isomers all have exact representations with four symmetries (and five for the para-isomer). The meta-isomer has the highest-error three-qubit representation, which we safely assume to be less than contributions of noise in this work.

4. Classical solution to the ACSE

In the fully quantum algorithm, the quantum computer is used in both the calculation of the ^2A and ^2D matrices. For the [4,4] cases we used a classical approach in solving for elements of ^2A, which reduces the computational demands on the quantum computer and yields sufficient accuracy in this case. This can be found by calculating elements of ^2A from

$$^2A_{j,l}^{i,k} = \langle \Psi | [\hat{a}_i^\dagger \hat{a}_k^\dagger \hat{a}_l \hat{a}_j, \hat{H}] | \Psi \rangle. \quad \text{(B6)}$$

More specifically, for a molecular system, the reduced Hamiltonian ^2K can be written as

$$^2K_{q,s}^{p,r} = \frac{1}{2(N-1)} \left[\delta_q^{p\,1}K_s^r + \delta_s^{r\,1}K_q^p + {}^2V_{q,s}^{p,r}(N-1) \right], \quad \text{(B7)}$$

and we define an operator $W_{q,s}^{p,r} = {}^2K_{q,s}^{p,r} - {}^2K_{s,q}^{p,r}$, which then leads to an expression for the total ACSE equation as [33,34]

$$
\begin{aligned}
{}^2A_{j,l}^{i,k} = &\sum_{p,q} \left({}^2D_{i,k}^{p,q} W_{j,l}^{p,q} - {}^2D_{j,l}^{p,q} W_{i,k}^{p,q} \right) \\
&+ \sum_{pqr} \left({}^3D_{j,l,q}^{p,r,k} W_{i,q}^{p,r} - {}^3D_{j,l,q}^{p,r,i} W_{k,q}^{p,r} - {}^3D_{r,q,j}^{i,k,p} W_{r,q}^{p,l} \right. \\
&\left. + {}^3D_{r,q,l}^{i,k,p} W_{r,q}^{p,j} \right).
\end{aligned} \quad \text{(B8)}
$$

Notably, this expression involves the 3-RDM, which can be reconstructed from its cumulant expansion [61]

$$^3D_{p,q,s}^{i,j,k} = 6\,{}^1D_p^i \wedge {}^1D_q^j \wedge {}^1D_s^k + 9\,{}^2\Delta_{p,q}^{i,j} \wedge {}^1D_s^k + {}^3\Delta_{p,q,s}^{i,j,k}. \quad \text{(B9)}$$

Here, the wedge product denotes the Grassmannian operator, combining antisymmetric permutations of upper and lower indices and dividing by the total number of permutations,

TABLE IV. Energetic error results (millihartrees) for different convergence thresholds and qubit representations for the QACSE with a quantum solution of the ACSE (or measured 3-RDM) for the ortho-, meta-, and para-benzyne configurations. The number of qubits refers to the qubit representation and related symmetries utilized, which for ortho and meta have nonzero errors. Values of $||^2A||$ refer to the convergence criteria, which is the norm of the ^2A matrix.

	Energy error relative to CASSCF (mhartree)								
	ortho			meta			para		
Qubits/$||^2A||$	0.05	0.01	0.001	0.05	0.01	0.001	0.05	0.01	0.001
3	1.393	1.393	0.916	11.197	1.108	0.869	0.284	0.284	0.003
4	2.957	0.033	0.006	10.563	0.363	0.115	0.284	0.284	0.003
8	13.634	0.200	0.008	14.042	0.240	0.101	5.711	0.042	0.005

TABLE V. Error in energy results (millihartree) for different convergence thresholds and qubit representations for the QACSE algorithm with a reconstructed 3-RDM. The number of qubits refers to the qubit representation and related symmetries utilized. Instead of the norm of the ^2A matrix, we use a trust region and energetic increase stopping criteria. We also indicate whether or not all of the elements of the ^2A matrix are implemented.

		Energy error relative to CASSCF (mhartree)					
		ortho		meta		para	
Trust criterion	Entire ^2A	3Q	4Q	3Q	4Q	3Q	4Q
5×10^{-2}	No	1.113	1.112	4.913	4.174	5.675	5.675
1×10^{-3}	No	1.113	1.112	2.975	2.077	1.231	1.234
1×10^{-6}	No	1.113	1.112	2.976	2.077	0.267	0.269
1×10^{-6}	Yes	1.126	0.181	3.687	3.002	0.182	0.182

$^n\Delta$ represents the nth-order reduced cumulant matrix, and we assume that $^3\Delta = 0$.

5. Simulated quantum results

Using the above schemes, we can provide simulated results without noise of the different benzyne isomers. Table IV shows simulated results with the quantum solution of the ACSE at different convergence criteria and number of qubits. Table V shows similar results where the evaluation of the ACSE residual on the quantum computer is replaced by a classical evaluation including classical reconstruction of the 3-RDM from the 2-RDM by a cumulant expansion.

In Table IV, we can see that with more strict convergence criteria, we are able to obtain highly accurate results for our given representation. Because there is error in the three- and four-qubit simulations, given a low norm in ^2A (which is taken relative to the truncated Hamiltonian operator and not the reduced Hamiltonian matrix ^2K), these results return essentially the approximation in the ortho and meta cases (0.92 and 0.87 mhartree, respectively). Additionally, these results show the most ideal case for the QACSE algorithm with the current choice of tapering, highlighting its potential on beyond-NISQ devices.

If we consider the systems with a reconstructed 3-RDM, as seen in Table V, we note several differences. Because the ^2A matrix from the reconstructed 3-RDM does not represent the true gradient, we use one-dimensional trust-region convergence criteria for our convergence threshold as in previ-

ous work. The criteria are (1) the quadratic model of the trust region, and (2) the error in the energy. In some cases we also trim the ^2A matrix in generating the *Ansatz*: discard elements in our current iteration that are below a given threshold (in this case, 0.5). If we do not trim the operator, then all of the terms are utilized.

These results are not unexpected, as errors from cumulant reconstruction in the literature are often in the single mhartree region. It also is possible that on a quantum computer the disconnect between an exact 2-RDM and inexact ^2A leads to an increase in errors. Unlike the quantum ACSE, here the four-qubit results match the full-qubit result for each instance, and so the latter are not reported. The ortho and para calculations achieve good accuracy, while the meta appears to have slightly more error. Despite this, the results recover the majority of the correlation energy, demonstrating that the reconstructed approach is not unsuitable for noisy simulations where errors are generally much larger than 1 mhartree.

6. Circuit implementations

Once the ^2A matrix is obtained for each step, we use a threshold to truncate the operator, and at each step add only one or two additional fermionic terms. As mentioned in the main text, the circuits are constructed by expressing $e^{\epsilon_n A_n}$ as a first-order Trotterization, resulting in products of exponentials Pauli strings which can be realized generally with CNOT gates and single-qubit rotations. In some instances we see a reduction in the number of two-qubit gates by using the following single-qubit identity:

$$e^{i\pi} U^\dagger \sigma_j U = \begin{cases} \sigma_x & \text{if } j = x, \\ \sigma_y & \text{if } j = z, \\ \sigma_z & \text{if } j = y, \end{cases} \quad \text{(B10)}$$

where $U = S^\dagger H S$. This can just as easily be applied to exponential transformations as well, and with this, we can transform an operator such as $e^{\alpha(X_1 X_2 + Y_1 Y_2)}$, which is expressed in three or four CNOT gates, to $U^\dagger e^{\alpha(X_1 X_2 + Z_1 Z_2)} U$ which can be expressed with only two CNOT gates. In general, we utilize straightforward concatenation techniques which possibly reduced the CNOT gates while preserving the connectivity of the device (which is linear).

While performing simulations under noiseless, stochastic, and simulated devicelike noise, we examined the pool of required operators, and then performed simplifications to reduce the number of CNOT gates that were involved. While in general this is not required, for optimal performance on near-term devices circuit simplifications are critical. Different

TABLE VI. Calibration data for the IBMQ-Rome device taken on November 9th, 2020, from randomized benchmarking of the qubit gates. The gate lengths for the U_2 and U_3 gates were 35 and 71 ns, respectively.

Qubit i	Frequency (GHz)	U_2 10^{-4}	U_3 10^{-4}	$RO_{0|1}$ 10^{-2}	$RO_{1|0}$ 10^{-2}	T_1 (μs)	T_2 (μs)	$[j]$ CNOT$_i^j$ (gate length) 10^{-2} (ns)
0	4.969	2.4	4.7	2.0	0.6	92.0	66.3	[1] 0.7 (320)
1	4.770	2.9	5.7	4.9	3.4	104.1	68.3	[0] 0.7 (356) [2] 2.0 (1109)
2	5.015	3.5	7.1	7.0	2.2	74.3	155.0	[1] 2.0 (1145) [3] 1.0 (377)
3	5.259	5.8	11.7	3.2	1.0	67.7	101.1	[2] 1.0 (341) [4] 1.6 (476)
4	4.997	2.7	5.3	1.6	0.7	50.1	103.0	[3] 1.6 (512)

TABLE VII. Calibration data taken for IBMQ-Bogota from December 4th to 7th, 2020, from benchmarking. See Table VI for descriptions. The gate lengths for the U_2 and U_3 gates were 35 and 71 ns, respectively.

Qubit i	Frequency (GHz)	U_2 10^{-4}	U_3 10^{-4}	$RO_{0\|1}$ 10^{-2}	$RO_{1\|0}$ 10^{-2}	T_1 (μs)	T_2 (μs)	$[j]$ $CNOT_i^j$ (gate length) 10^{-2} (ns)
				$12 - 04 - 20$				
0	5.000	4.8	9.6	4.0	1.4	93.5	141.4	[1] 1.7 (690)
1	4.845	2.2	4.4	4.4	2.9	134.4	76.1	[0] 1.7 (654) [2] 0.7 (498)
2	4.783	1.7	3.4	4.9	1.5	128.2	206.2	[1] 0.7 (533) [3] 3.3 (626)
3	4.858	15.7	31.3	4.6	1.2	84.6	36.8	[2] 3.3 (590) [4] 2.5 (370)
4	4.978	4.2	8.3	4.9	1.6	50.9	87.1	[3] 2.5 (334)
				$12 - 05 - 20$				
0	5.000	3.0	6.1	3.7	1.3	91.5	119.8	[1] 1.7 (690)
1	4.845	2.6	5.2	4.3	3.3	137.4	75.4	[0] 1.7 (654) [2] 0.8 (498)
2	4.783	1.5	3.0	3.3	1.3	133.0	226.5	[1] 0.8 (533) [3] 0.6 (626)
3	4.858	1.6	3.3	3.4	0.6	159.7	244.4	[2] 0.6 (590) [4] 0.8 (370)
4	4.978	1.9	3.9	2.8	1.0	107.3	146.1	[3] 0.8 (334)
				$12 - 06 - 20$				
0	5.000	3.5	7.0	5.3	1.6	88.2	107.7	[1] 1.8 (690)
1	4.845	2.4	4.9	3.8	2.2	145.0	95.8	[0] 1.8 (654) [2] 0.7 (498)
2	4.783	1.8	3.6	4.7	1.4	165.0	211.2	[1] 0.7 (533) [3] 0.6 (626)
3	4.858	2.6	5.2	1.9	0.7	160.2	311.7	[2] 0.6 (590) [4] 0.7 (370)
4	4.978	1.9	3.8	3.6	1.2	126.0	149.4	[3] 0.7 (334)
				$12 - 07 - 20$				
0	5.000	3.5	7.0	8.2	1.6	44.8	55.7	[1] 1.8 (690)
1	4.845	2.4	4.9	4.7	2.6	178.2	98.8	[0] 1.8 (654) [2] 0.8 (498)
2	4.783	1.8	3.6	3.9	0.9	126.0	231.0	[1] 0.8 (533) [3] 0.8 (626)
3	4.858	2.6	5.2	2.8	0.4	124.0	168.6	[2] 0.8 (590) [4] 0.9 (370)
4	4.978	1.9	3.8	3.9	1.3	93.5	188.0	[3] 0.9 (334)

compilation methods were attempted, but ultimately (likely due to the connectivity constraints of the devices), manual simplifications yielded lower CNOT counts. The symmetries have the effect of reducing the number of nonzero excitation operators, as certain excitation sequences act outside the symmetry state. Acting on the imaginary elements of the 2-RDM, we can find the nonzero elements and then prepare circuits accordingly. For the three-qubit case this resulted in six unique Pauli strings. A similar procedure was carried out with the four-qubit case, although we found that we did not have to prepare the entire pool of operators.

7. Quantum device specifications

For the quantum computation we used three different quantum devices. For the single-qubit simulation, we used IBMQ-Rome (five-qubit device), whereas for the three- and four-qubit calculations we used IBMQ-Bogota as well as IBMQ-Santiago, which are same generation linearly connected five-qubit devices. These were accessed through the IBM Quantum Experience. The quantum devices use fixed-frequency transmon qubits with coplanar waveguide resonators [98,99]. The Python package QISKIT(v 0.15.0, 0.17.1) [100] was used to interface with the device. Device properties can be found in Tables VI–VIII.

U_2 and U_3 represent single-qubit gate errors containing one and two $X_{\pi/2}$ pulses and two and three frame changes respectively. Newer devices (see Table VIII) directly express these as rotations using the $\sqrt{X}$ and X gates with intermediate frame changes representing rotations along the z axis. $RO_{i|j}$ represents the probability of measuring the state i given a prepared state j. T_1 and T_2 are the given thermal relaxation times for each qubit. Frequency refers to the qubits operational frequency, and influences the excited-state population based on the device temperature. $[j]$ specifies the target qubit with control qubit i, and the number in parentheses after each entry in the CNOT column indicates the gate length. The

TABLE VIII. Calibration data taken for IBMQ-Santiago from August 24th. The gate lengths for the $\sqrt{X}$ and X gates are both 35 ns. Santiago was used to calculate the three-qubit meta-isomer calculation.

Qubit i	Frequency (GHz)	$\sqrt{X}$ 10^{-4}	X 10^{-4}	$RO_{0\|1}$ 10^{-2}	$RO_{1\|0}$ 10^{-2}	T_1 (μs)	T_2 (μs)	$[j]$ $CNOT_i^j$ (gate length) 10^{-2} (ns)
2	4.821	2.0	2.0	1.5	0.5	99.0	89.8	[3] 0.7 (377)
3	4.742	3.0	3.0	1.4	0.5	75.7	67.4	[2] 0.7 (412) [4] 0.7 (377)
4	4.816	1.6	1.6	2.2	1.0	99.5	155.1	[3] 0.7 (341)

gate lengths for the U_2 and U_3 gates were 35 and 71 ns, respectively.

APPENDIX C: ERROR-MITIGATION METHODS

To directly mitigate the effects of noise on the quantum computer, we use a variety of techniques in addition to the ones listed in the main text (limit-preserving correction and the purification of the 2-RDM).

1. Number-preserving projection to diagonal elements of the 2-RDM

The most effective error correction comes by filtering diagonal elements of the 2-RDM, of the form $^2D_{p,q}^{p,q}$, so that the number operator is preserved. Because these elements commute with single-qubit measurements that are performed, they can be filtered according to the measurement result. Counts that have differing values of N or S_z are rejected, and so we are filtered to a set of RDMs with the proper trace and projected spin properties [i.e., $\mathrm{Tr}\,^2D = N(N-1)$]. While heavily erroneous off-diagonal elements can also lead to non-physical eigenvalues [4], correcting for these in the 2-RDM case is not straightforward and likely would not reduce the overall errors.

2. Measurement correction of prepared states (SPAM)

Finally, the state preparation and measurement, which involves preparing all possible quantum states for some qubit space, and constructing a transition matrix with the associated inverse, was utilized to mitigate measurement errors. We applied this to local qubits, and so did not correct for correlated measurement errors. This procedure has been documented in many places [105,106] and can be implemented through QISKIT.

3. Limit-preserving correction for an iterative *Ansatz*

In the main text we described our error-mitigation strategy which we denoted as a limit-preserving correction for an iterative *Ansatz*, and described the framework or context in
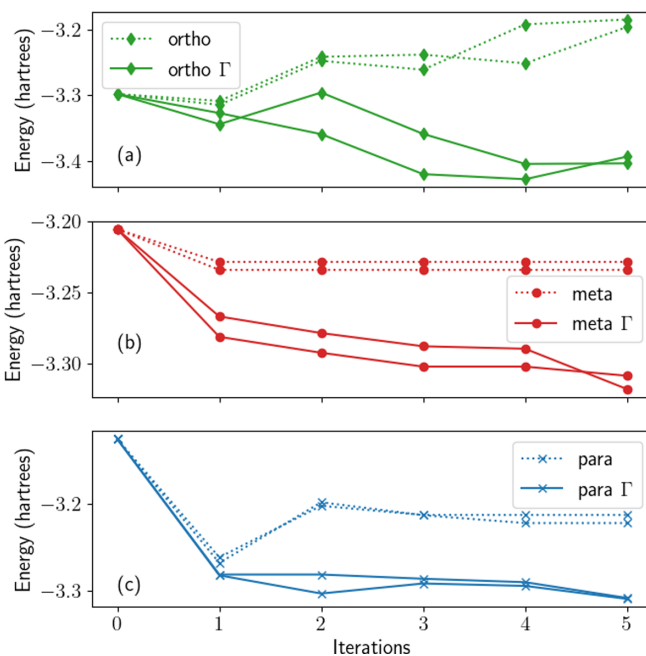

FIG. 6. Two optimization attempts for (a) ortho-, (b) meta-, and (c) para-benzyne configurations with and without the $^2\Gamma$-preserving correction showing the first five iterations. In the meta-isomer case without the $^2\Gamma$ correction, unfavorable steps in choosing ϵ_n are rejected and so the run plateaus after the first step.

which it could be useful. To illustrate these points, Figure 6 highlights the effect of performing a traditional (three-qubit) calculation with an iterative design, versus a $^2\Gamma$-corrected result. The increasing energy can be seen in each iteration with the standard result. For each isomer, only 1 step can be taken before the *Ansatz* is too corrupted to provide a reasonable ground state. However, though the optimization with the $^2\Gamma$ correction is still noisy, and not always smooth, we are able to keep or improve upon the energy gains in each case, and achieve results closer to the true ground state.

[1] I. Kassal, J. D. Whitfield, A. Perdomo-Ortiz, M.-h. Yung, and A. Aspuru-Guzik, Simulating chemistry using quantum computers, Annu. Rev. Phys. Chem. **62**, 185 (2011).

[2] P. J. J. O'Malley, R. Babbush, I. D. Kivlichan, J. Romero, J. R. McClean, R. Barends, J. Kelly, P. Roushan, A. Tranter, N. Ding, B. Campbell, Y. Chen, Z. Chen, B. Chiaro, A. Dunsworth, A. G. Fowler, E. Jeffrey, E. Lucero, A. Megrant, J. Y. Mutus *et al.*, Scalable Quantum Simulation of Molecular Energies, Phys. Rev. X **6**, 031007 (2016).

[3] S. McArdle, S. Endo, A. Aspuru-Guzik, S. C. Benjamin, and X. Yuan, Quantum computational chemistry, Rev. Mod. Phys. **92**, 015003 (2020).

[4] F. Arute, K. Arya, R. Babbush, D. Bacon, J. C. Bardin, R. Barends, S. Boixo, M. Broughton, B. B. Buckley, and D. A. E. A. Buell, Hartree-Fock on a superconducting qubit quantum computer, Science **369**, 1084 (2020).

[5] A. Aspuru-Guzik, A. D. Dutoi, P. J. Love, and M. Head-Gordon, Simulated quantum computation of molecular energies, Science **309**, 1704 (2005).

[6] S. Lloyd, Universal quantum simulators, Science **273**, 1073 (1996).

[7] D. Lu, B. Xu, N. Xu, Z. Li, H. Chen, X. Peng, R. Xu, and J. Du, Quantum chemistry simulation on quantum computers: theories and experiments, Phys. Chem. Chem. Phys. **14**, 9411 (2012).

[8] V. E. Elfving, B. W. Broer, M. Webber, J. Gavartin, M. D. Halls, K. P. Lorton, and A. Bochevarov, How will quantum computers provide an industrially relevant computational advantage in quantum chemistry? arXiv:2009.12472.

[9] T. Helgaker, P. Jørgensen, and J. Olsen, *Molecular Electronic-Structure Theory* (Wiley, Chichester, UK, 2000), p. 908.

[10] H. Lischka, D. Nachtigallová, A. J. Aquino, P. G. Szalay, F. Plasser, F. B. MacHado, and M. Barbatti, Multireference

approaches for excited states of molecules, Chem. Rev. **118**, 7293 (2018).

[11] F. A. Evangelista, Perspective: Multireference coupled cluster theories of dynamical electron correlation, J. Chem. Phys. **149**, 030901 (2018).

[12] J. Preskill, Quantum Computing in the NISQ era and beyond, Quantum **2**, 79 (2018).

[13] K. Head-Marsden, J. Flick, C. J. Ciccarino, and P. Narang, Quantum information and algorithms for correlated quantum matter, Chem. Rev. **5**, 3061 (2020).

[14] A. Peruzzo, J. McClean, P. Shadbolt, M.-H. Yung, X.-Q. Zhou, P. J. Love, A. Aspuru-Guzik, and J. L. O'Brien, A variational eigenvalue solver on a photonic quantum processor, Nat. Commun. **5**, 4213 (2014).

[15] J. R. McClean, J. Romero, R. Babbush, and A. Aspuru-Guzik, The theory of variational hybrid quantum-classical algorithms, New J. Phys. **18**, 023023 (2016).

[16] A. Kandala, A. Mezzacapo, K. Temme, M. Takita, M. Brink, J. M. Chow, and J. M. Gambetta, Hardware-efficient variational quantum eigensolver for small molecules and quantum magnets, Nature (London) **549**, 242 (2017).

[17] A. Kandala, K. Temme, A. D. Córcoles, A. Mezzacapo, J. M. Chow, and J. M. Gambetta, Error mitigation extends the computational reach of a noisy quantum processor, Nature (London) **567**, 491 (2019).

[18] E. Fontana, N. Fitzpatrick, D. M. Ramo, R. Duncan, and I. Rungger, Evaluating the noise resilience of variational quantum algorithms, Phys. Rev. A **104**, 022403 (2021).

[19] S. McArdle, X. Yuan, and S. Benjamin, Error-Mitigated Digital Quantum Simulation, Phys. Rev. Lett. **122**, 180501 (2019).

[20] S. E. Smart and D. A. Mazziotti, Quantum-classical hybrid algorithm using an error-mitigating N-representability condition to compute the Mott metal-insulator transition, Phys. Rev. A **100**, 022517 (2019).

[21] X. Bonet-Monroig, R. Sagastizabal, M. Singh, and T. E. O'Brien, Low-cost error mitigation by symmetry verification, Phys. Rev. A **98**, 062339 (2018).

[22] S. E. Smart and D. A. Mazziotti, Quantum Solver of Contracted Eigenvalue Equations for Scalable Molecular Simulations on Quantum Computing Devices, Phys. Rev. Lett. **126**, 070504 (2021).

[23] D. A. Mazziotti, Contracted Schrödinger equation: Determining quantum energies and two-particle density matrices without wave functions, Phys. Rev. A **57**, 4219 (1998).

[24] H. Nakatsuji and K. Yasuda, Direct Determination of the Quantum-Mechanical Density Matrix Using the Density Equation, Phys. Rev. Lett. **76**, 1039 (1996).

[25] K. Yasuda and H. Nakatsuji, Direct determination of the quantum-mechanical density matrix using the density equation. II., Phys. Rev. A **56**, 2648 (1997).

[26] F. Colmenero and C. Valdemoro, Approximating q-order reduced density matrices in terms of the lower-order ones. II. applications, Phys. Rev. A **47**, 979 (1993).

[27] C. Valdemoro, L. M. Tel, E. Pérez-Romero, and D. R. Alcoba, Four new forms of the contracted Schrödinger equation and their connection with the second-order hypervirial condition, Int. J. Quantum Chem. **108**, 1090 (2008).

[28] D. A. Mazziotti, Variational method for solving the contracted schrodinger equation through a projection of the n-particle power method onto the two-particle space, J. Chem. Phys. **116**, 1239 (2002).

[29] D. A. Mazziotti, Comparison of contracted schrodinger and coupled-cluster theories, Phys. Rev. A **60**, 4396 (1999).

[30] A. J. Coleman and V. I. Yukalov, *Reduced Density Matrices: Coulson's Challenge* (Springer, Berlin, 2000).

[31] D. A. Mazziotti, Exactness of wave functions from two-body exponential transformations in many-body quantum theory, Phys. Rev. A **69**, 012507 (2004).

[32] D. A. Mazziotti, Exact two-body expansion of the many-particle wave function, Phys. Rev. A **102**, 030802(R) (2020).

[33] D. A. Mazziotti, Anti-Hermitian Contracted Schrödinger Equation: Direct Determination of the Two-Electron Reduced Density Matrices of Many-Electron Molecules, Phys. Rev. Lett. **97**, 143002 (2006).

[34] D. A. Mazziotti, Anti-Hermitian part of the contracted Schrödinger equation for the direct calculation of two-electron reduced density matrices, Phys. Rev. A **75**, 022505 (2007).

[35] G. Gidofalvi and D. A. Mazziotti, Direct calculation of excited-state electronic energies and two-electron reduced density matrices from the anti-Hermitian contracted Schrödinger equation, Phys. Rev. A **80**, 022507 (2009).

[36] D. Mukherjee and W. Kutzelnigg, Irreducible Brillouin conditions and contracted Schrödinger equations for n-electron systems. I. The equations satisfied by the density cumulants, J. Chem. Phys. **114**, 2047 (2001).

[37] F. A. Evangelista, G. K. L. Chan, and G. E. Scuseria, Exact parameterization of fermionic wave functions via unitary coupled cluster theory, J. Chem. Phys. **151**, 244112 (2019).

[38] R. Santagati, J. Wang, A. A. Gentile, S. Paesani, N. Wiebe, J. R. McClean, S. Morley-Short, P. J. Shadbolt, D. Bonneau, J. W. Silverstone, D. P. Tew, X. Zhou, J. L. O'Brien, and M. G. Thompson, Witnessing eigenstates for quantum simulation of Hamiltonian spectra, Sci. Adv. **4**, eaap9646 (2018).

[39] S. M. Robinson, *Numerical Optimization* (Springer, Berlin, 2006).

[40] P. Rakshit and A. Konar, *Principles in Noisy Optimization*, Cognitive Intelligence and Robotics (Springer, Singapore, 2018).

[41] A. Daskin and S. Kais, Group leaders optimization algorithm, Mol. Phys. **109**, 761 (2011).

[42] J. W. Snyder, A. E. Rothman, J. J. Foley, and D. A. Mazziotti, Conical intersections in triplet excited states of methylene from the anti-hermitian contracted Schrödinger equation, J. Chem. Phys. **132**, 154109 (2010).

[43] J. W. Snyder and D. A. Mazziotti, Photoexcited tautomerization of vinyl alcohol to acetylaldehyde via a conical intersection from contracted schrodinger theory, Phys. Chem. Chem. Phys. **14**, 1660 (2011).

[44] J. W. Snyder and D. A. Mazziotti, Photoexcited conversion of gauche-1,3-butadiene to bicyclobutane via a conical intersection: Energies and reduced density matrices from the anti-Hermitian contracted Schrödinger equation, J. Chem. Phys. **135**, 024107 (2011).

[45] L. Greenman and D. A. Mazziotti, Balancing single- and multi-reference correlation in the chemiluminescent reaction of dioxetanone using the anti-hermitian contracted schrodinger equation, J. Chem. Phys. **134**, 174110 (2011).

[46] A. M. Sand and D. A. Mazziotti, Enhanced computational efficiency in the direct determination of the two-electron reduced

density matrix from the anti-Hermitian contracted Schrödinger equation with application to ground and excited states of conjugated π -systems, J. Chem. Phys. **143**, 134110 (2015).

[47] D. R. Alcoba, C. Valdemoro, L. M. Tel, E. Pérez-Romero, and O. B. Oña, Optimized solution procedure of the G-particle-hole hypervirial equation for multiplets: Application to doublet and triplet states, J. Phys. Chem. A **115**, 2599 (2011).

[48] S. E. Smart, P. G. Scrape, L. J. Butler, and D. A. Mazziotti, Using reduced density matrix techniques to capture static and dynamic correlation in the energy landscape for the decomposition of the CH_2 CH_2 ONO radical and support a non-irc pathway, J. Chem. Phys. **149**, 024302 (2018).

[49] M. A. Nielsen and I. L. Chuang, *Quantum Computation and Quantum Information* (Cambridge University Press, Cambridge, 2010), p. 702.

[50] J. Romero, R. Babbush, J. R. McClean, C. Hempel, P. Love, and A. Aspuru-Guzik, Strategies for quantum computing molecular energies using the unitary coupled cluster ansatz, Quantum Sci. Technology **4**, 014008 (2018).

[51] J. Lee, W. J. Huggins, M. Head-Gordon, and K. B. Whaley, Generalized unitary coupled cluster wave functions for quantum computation, J. Chem. Theory Comput. **15**, 311 (2019).

[52] H. R. Grimsley, S. E. Economou, E. Barnes, and N. J. Mayhall, An adaptive variational algorithm for exact molecular simulations on a quantum computer, Nat. Commun. **10**, 3007 (2019).

[53] Y. Yang, D. Peng, E. R. Davidson, and W. Yang, Singlet-triplet energy gaps for diradicals from particle-particle random phase approximation, J. Phys. Chem. A **119**, 4923 (2015).

[54] J. Shee, E. J. Arthur, S. Zhang, D. R. Reichman, and R. A. Friesner, Singlet-triplet energy gaps of organic biradicals and polyacenes with auxiliary-field quantum monte carlo, J. Chem. Theory Comput. **15**, 4924 (2019).

[55] A. L. McManus, E. P. Hoy, and D. A. Mazziotti, Energies and structures in biradical chemistry from the parametric two-electron reduced-density matrix method: applications to the benzene and cyclobutadiene biradicals, Phys. Chem. Chem. Phys. **17**, 12521 (2015).

[56] S. G. Wierschke, J. J. Nash, and R. R. Squires, A multiconfigurational scf and correlation-consistent ci study of the structures, stabilities, and singlet-triplet splittings of o-, m-, and p-benzyne, J. Am. Chem. Soc. **115**, 11958 (1993).

[57] S. L. Debbert and C. J. Cramer, Systematic comparison of the benzynes, pyridynes, and pyridynium cations and characterization of the Bergman cyclization of Z-but-1-en-3-yn-1-y1 isonitrile to the meta diradical 2,4-pyridyne, Int. J. Mass Spectrom. **201**, 1 (2000).

[58] J. J. Nash and R. R. Squires, Theoretical studies of o-, m-, and p-benzyne negative ions, J. Am. Chem. Soc. **118**, 11872 (1996).

[59] J. J. Foley and D. A. Mazziotti, Measurement-driven reconstruction of many-particle quantum processes by semidefinite programming with application to photosynthetic light harvesting, Phys. Rev. A **86**, 012512 (2012).

[60] N. C. Rubin, R. Babbush, and J. McClean, Application of fermionic marginal constraints to hybrid quantum algorithms, New J. Phys. **20**, 053020 (2018).

[61] D. A. Mazziotti, Approximate solution for electron correlation through the use of Schwinger probes, Chem. Phys. Lett. **289**, 419 (1998).

[62] A. E. Deprince and D. A. Mazziotti, Cumulant reconstruction of the three-electron reduced density matrix in the anti-Hermitian contracted Schrödinger equation, J. Chem. Phys. **127**, 104104 (2007).

[63] W. Kutzelnigg and D. Mukherjee, Cumulant expansion of the reduced density matrices, J. Chem. Phys. **110**, 2800 (1999).

[64] J. P. Misiewicz, J. M. Turney, and H. F. Schaefer, Reduced density matrix cumulants: The combinatorics of size-consistency and generalized normal ordering, J. Chem. Theory Comput. **16**, 6150 (2020).

[65] D. A. Mazziotti, Purification of correlated reduced density matrices, Phys. Rev. E **65**, 026704 (2002).

[66] C. Garrod and J. K. Percus, Reduction of the N-Particle Variational Problem, J. Math. Phys. **5**, 1756 (1964).

[67] A. J. Coleman, Structure of fermion density matrices, Rev. Mod. Phys. **35**, 668 (1963).

[68] R. M. Erdahl, Representability, Int. J. Quantum Chem. **13**, 697 (1978).

[69] L. Vandenberghe and S. Boyd, Semidefinite programming, SIAM Rev. **38**, 49 (1996).

[70] D. A. Mazziotti, Large-Scale Semidefinite Programming for Many-Electron Quantum Mechanics, Phys. Rev. Lett. **106**, 083001 (2011).

[71] D. A. Mazziotti, Realization of Quantum Chemistry without Wave Functions through First-Order Semidefinite Programming, Phys. Rev. Lett. **93**, 213001 (2004).

[72] *Advances in Chemical Physics*, edited by D. A. Mazziotti (Wiley, Hoboken, NJ, 2007), Vol. 134, p. 574.

[73] J. M. Montgomery and D. A. Mazziotti, Strong electron correlation in nitrogenase cofactor, femoco, J. Phys. Chem. A **122**, 4988 (2018).

[74] J. N. Boyn, J. N. Boyn, J. Xie, J. S. Anderson, D. A. Mazziotti, and D. A. Mazziotti, Entangled electrons drive a non-superexchange mechanism in a cobalt quinoid dimer complex, J. Phys. Chem. Lett. **11**, 4584 (2020).

[75] W. Sander, m-benzyne and p-benzyne, Acc. Chem. Res. **32**, 669 (1999).

[76] S. P. Ross and T. R. Hoye, Reactions of hexadehydro-diels–alder benzynes with structurally complex multifunctional natural products, Nat. Chem. **9**, 523 (2017).

[77] F. Shi, J. P. Waldo, Y. Chen, and R. C. Larock, Benzyne click chemistry: Synthesis of benzotriazoles from benzynes and azides, Org. Lett. **10**, 2409 (2008).

[78] A. V. Dubrovskiy, N. A. Markina, and R. C. Larock, Use of benzynes for the synthesis of heterocycles, Org. Biomol. Chem. **11**, 191 (2013).

[79] P. G. Wenthold, R. R. Squires, and W. C. Lineberger, Ultraviolet photoelectron spectroscopy of the o-, m-, and p-benzyne negative ions. electron affinities and singlet-triplet splittings for o-, m-, and p-benzyne, J. Am. Chem. Soc. **120**, 5279 (1998).

[80] Y. A. Bernard, Y. Shao, and A. I. Krylov, General formulation of spin-flip time-dependent density functional theory using non-collinear kernels: Theory, implementation, and benchmarks, J. Chem. Phys. **136**, 204103 (2012).

[81] L. V. Slipchenko and A. I. Krylov, Singlet-triplet gaps in diradicals by the spin-flip approach: A benchmark study, J. Chem. Phys. **117**, 4694 (2002).

[82] J.-N. Boyn, A. O. Lykhin, S. E. Smart, L. Gagliardi, and D. A. Mazziotti, Quantum-classical hybrid algorithm for the

simulation of all-electron correlation, J. Chem. Phys. **155**, 244106 (2021).

[83] S. E. Smart and D. A. Mazziotti, Efficient two-electron ansatz for benchmarking quantum chemistry on a quantum computer, Phys. Rev. Res. **2**, 023048 (2020).

[84] S. Bravyi, J. M. Gambetta, A. Mezzacapo, and K. Temme, Tapering off qubits to simulate fermionic Hamiltonians, arXiv:1701.08213.

[85] K. Temme, S. Bravyi, and J. M. Gambetta, Error Mitigation for Short-Depth Quantum Circuits, Phys. Rev. Lett. **119**, 180509 (2017).

[86] H. Nakatsuji, Structure of the exact wave function, J. Chem. Phys. **113**, 2949 (2000).

[87] M. Nooijen, Can the Eigenstates of a Many-Body Hamiltonian Be Represented Exactly Using a General Two-Body Cluster Expansion? Phys. Rev. Lett. **84**, 2108 (2000).

[88] T. V. Voorhis and M. Head-Gordon, Two-body coupled cluster expansions, J. Chem. Phys. **115**, 5033 (2001).

[89] H. Nakatsuji, Structure of the exact wave function. III. Exponential ansatz, J. Chem. Phys. **115**, 2465 (2001).

[90] E. R. Davidson, Exactness of the General Two-Body Cluster Expansion in Many-Body Quantum Theory, Phys. Rev. Lett. **91**, 123001 (2003).

[91] S. Ronen, Can the Eigenstates of a Many-Body Hamiltonian Be Represented Exactly Using a General Two-Body Cluster Expansion? Phys. Rev. Lett. **91**, 123002 (2003).

[92] P. Piecuch, K. Kowalski, P.-D. Fan, and K. Jedziniak, Exactness of Two-Body Cluster Expansions in Many-Body Quantum Theory, Phys. Rev. Lett. **90**, 113001 (2003).

[93] W. Kutzelnigg and D. Mukherjee, Minimal parametrization of an n-electron state, Phys. Rev. A **71**, 022502 (2005).

[94] Maplesoft, a division of Waterloo Maple Inc., Waterloo, Ontario, Maple.

[95] RDMCHEM, Chicago, Illinois, Quantum chemistry toolbox.

[96] Q. Sun, T. C. Berkelbach, N. S. Blunt, G. H. Booth, S. Guo, Z. Li, J. Liu, J. D. McClain, E. R. Sayfutyarova, S. Sharma, S. Wouters, and G. K.-L. Chan, Pyscf: the python-based simulations of chemistry framework, WIREs Comput. Mol. Sci. **8**, e1340 (2018).

[97] T. H. Dunning, Gaussian basis sets for use in correlated molecular calculations. i. the atoms boron through neon and hydrogen, J. Chem. Phys. **90**, 1007 (1989).

[98] J. Koch, T. M. Yu, J. Gambetta, A. A. Houck, D. I. Schuster, J. Majer, A. Blais, M. H. Devoret, S. M. Girvin, and R. J. Schoelkopf, Charge-insensitive qubit design derived from the Cooper pair box, Phys. Rev. A **76**, 042319 (2007).

[99] J. M. Chow, A. D. Córcoles, J. M. Gambetta, C. Rigetti, B. R. Johnson, J. A. Smolin, J. R. Rozen, G. A. Keefe, M. B. Rothwell, M. B. Ketchen, and M. Steffen, Simple All-Microwave Entangling Gate for Fixed-Frequency Superconducting Qubits, Phys. Rev. Lett. **107**, 080502 (2011).

[100] M. Treinish, J. Gambetta, P. Nation, P. Kassebaum, qiskit-bot, D. M. Rodrguez, S. de la Puente Gonzlez, S. Hu, K. Krsulich, L. Zdanski *et al.*, Qiskit/qiskit: Qiskit 0.34.1 (0.34.1), 2022, doi:10.5281/zenodo.2573505.

[101] S. E. Smart and D. A. Mazziotti, Lowering tomography costs in quantum simulation with a symmetry projected operator basis, Phys. Rev. A **103**, 012420 (2021).

[102] S. E. Smart and D. A. Mazziotti, hqca: hybrid quantum computing algorithms for quantum chemistry.

[103] K. Setia, R. Chen, J. E. Rice, A. Mezzacapo, M. Pistoia, and J. D. Whitfield, Reducing qubit requirements for quantum simulations using molecular point group symmetries, J. Chem. Theory Comput. **16**, 6091 (2020).

[104] D. Gottesman, Stabilizer codes and quantum error correction, arXiv:quant-ph/9705052.

[105] H. P. Breuer and F. Petruccione, *The Theory of Open Quantum Systems* (Oxford University Press, Oxford, 2007), pp. 1–656.

[106] L. C. Govia, G. J. Ribeill, D. Ristè, M. Ware, and H. Krovi, Bootstrapping quantum process tomography via a perturbative ansatz, Nat. Commun. **11**, 1084 (2020).